# Anisotropic Dzyaloshinskii-Moriya interaction in ultrathin epitaxial Au/Co/W(110)

Lorenzo Camosi,[1,*] Stanislas Rohart,[2] Olivier Fruchart,[1,3] Stefania Pizzini,[1] Mohamed Belmeguenai,[4] Yves Roussigné,[4] Andreï Stashkevich,[4,5] Salim Mourad Cherif,[4] Laurent Ranno,[1] Maurizio de Santis,[1] and Jan Vogel[1]

[1] *Université Grenoble Alpes, CNRS, Institut Néel, F-38000 Grenoble, France*

[2] *Laboratoire de Physique des Solides, Université Paris-Sud, CNRS UMR 8502, F-91405 Orsay Cedex, France*

[3] *Univversité Grenoble Alpes, CNRS, CEA, Grenoble INP, SPINTEC, F-38000 Grenoble, France*

[4] *LSPM-CNRS, Université Paris XIII-Sorbonne Paris Cité, F-93430 Villetaneuse, France*

[5] *International laboratory "MultiferrLab", ITMO University, St. Petersburg, Russia*

(Received 5 January 2017; revised manuscript received 23 May 2017; published 27 June 2017)

We used Brillouin light scattering spectroscopy to independently determine the in-plane magnetocrystalline anisotropy and the Dzyaloshinskii-Moriya interaction (DMI) in out-of-plane magnetized Au/Co/W(110). We found that the DMI strength is 2–3 times larger along the bcc[$\bar{1}$10] than along the bcc[001] direction. We use analytical considerations to illustrate the relationship between the crystal symmetry of the stack and the anisotropy of microscopic DMI. Such an anisotropic DMI is the first step to realize isolated elliptical skyrmions or antiskyrmions in thin-film systems with $C_{2v}$ symmetry.

DOI: 10.1103/PhysRevB.95.214422

## I. INTRODUCTION

An antisymmetric exchange interaction, the Dzyaloshinskii -Moriya interaction (DMI), was theoretically predicted by Dzyaloshinskii [1] using symmetry arguments in bulk magnetic systems. Then Moriya [2] demonstrated the antisymmetric spin coupling in systems with a lack of inversion symmetry by including spin-orbit coupling in the superexchange interaction. Fert and Levy [3] pointed out that high spin-orbit scattering centers can break the indirect exchange symmetry. DMI presents particular interest since it can stabilize chiral magnetic textures like skyrmions and antiskyrmions [4], magnetic solitons with a chiral vortexlike spin configuration which are characterized by a topological charge $N_{\mathrm{sk}}$. In a continuous-field approximation $N_{\mathrm{sk}}$ can be formulated as the integral on the space $(r,\alpha)$ that counts how many times the magnetization $\mathbf{m}(\phi(\alpha),\theta(r))$ [Fig. 1(c)] wraps the unit sphere [5]:

$$N_{\mathrm{sk}} = \frac{1}{4\pi}\int \frac{d\theta}{dr}\frac{d\phi}{d\alpha}\sin\theta\, dr\, d\alpha = Wp = \pm 1 \qquad (1)$$

where $p$ describes the direction of the core of the spin texture [$p = 1(-1)$ if $\theta(r=0) = 0(\pi)$] and $W = [\phi(\alpha)]_{\alpha=0}^{\alpha=2\pi}/2\pi = \pm 1$ is the winding number. Considering the same magnetization background, i.e., the same $p$ value, skyrmions [$\phi(\alpha) \propto \alpha$] and antiskyrmions [$\phi(\alpha) \propto -\alpha$] have opposite winding numbers and hence opposite topological charges. The spin modulation $\phi(\alpha)$, and hence the winding number, depends on the DMI symmetry that in a monocrystalline system directly arises from the crystal symmetry [6,7].

Circular skyrmions in an isotropic DMI environment have experimentally been observed in bulk systems with B20 symmetry [8] and as metastable objects in ultrathin magnetic films [9–11]. Skyrmions can also display a noncylindrical symmetry in anisotropic environments. The effect of spatially modulated exchange energy and magnetocrystalline anisotropy on the skyrmion shape has been theoretically analyzed [12,13] and experimentally investigated [14] in ultrathin films, while a distorted skyrmion lattice [15] due to an anisotropic DMI has been evidenced in a mechanically strained single crystal.

Antiskyrmions have been theoretically predicted in bulk systems where the $D_{2d}$ and $S_4$ [6] symmetry induces an anisotropic DMI with inversion of chirality between perpendicular directions. They have been theoretically investigated as metastable states at an energy higher than the skyrmion in ultrathin films with isotropic chirality [16] and in systems without DMI [17].

This paper consists of two parts. In the first part, we experimentally study thin epitaxial Co films on W(110). We use Brillouin light scattering (BLS) spectroscopy to show that the $C_{2v}$ crystal symmetry leads to a strong anisotropy of the DMI, with a value which is 2–3 times higher along the bcc[$\bar{1}$10] direction than along the bcc[001] direction. In the second part, we first show the relationship between the atomic DMI at the W\Co interface and the micromagnetic DMI in a $C_{2v}$ symmetry system. Then, we analyze the spin waves and spin configurations stabilized by the anisotropic DMI energy in a general $C_{2v}$ symmetry in order to explain our BLS measurements. Finally, we show that a DMI with opposite sign along two perpendicular in-plane directions should lead to the stabilization of antiskyrmions.

## II. SAMPLE GROWTH

The sample stack is grown by pulsed laser deposition, and crystallographic properties are investigated *in situ*. The (11$\bar{2}$0) surface of a commercial $Al_2O_3$ single crystal is used as the substrate for growing at room temperature a thin film of Mo (0.8 nm) followed by the deposition of an 8-nm-thick W film. The stack is then annealed at 1200 K for 1 h. During this annealing the Mo underlayer promotes the selection of a unique epitaxial relationship, avoiding twins and yielding a single-crystalline film [18]. Reflection high-energy electron diffraction (RHEED), shown in the Supplemental Material [19], confirms the disappearance of the W twins and the correct epitaxial relationship (Fig. 1). A Co film with a

*lorenzo.camosi@neel.cnrs.fr

 

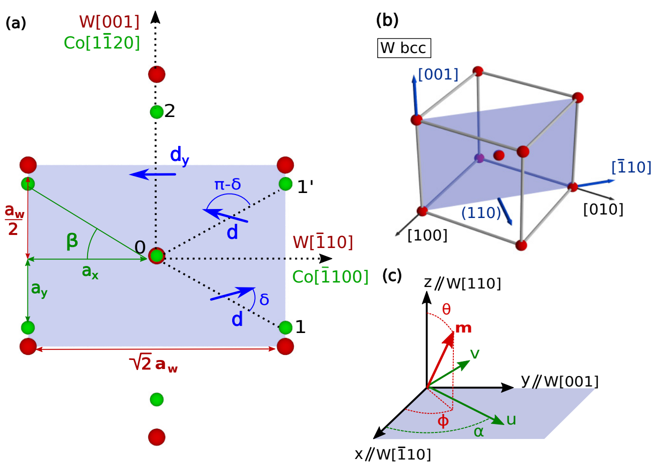


FIG. 1. (a) Superposition of the W(110) and the strained Co(0001) surfaces with the Nishiyama-Wassermann relationship. (b) Tungsten bcc unit cell with the (110) surface highlighted. (c) Illustration of the geometry and notation used to describe the magnetization $(\theta;\phi)$ and the directions $\alpha$ in the bcc(110) crystal framework.

thickness $t = 0.65$ nm is then deposited. The best condition for layer-by-layer growth is obtained by progressively warming the sample from room temperature to 350 K while the Co thickness increases from 0 to 0.65 nm. The immiscibility between Co and W guarantees a flat and sharp interface. RHEED and grazing incidence x-ray diffraction (GIXRD) patterns [19] demonstrate the retained single-crystal feature through the Nishiyama-Wassermann epitaxial relationship. The lattice misfits along the main in-plane crystallographic directions are $\Delta a_{bcc[\bar{1}10]} = \frac{\sqrt{2}a_W - \sqrt{3}a_{Co}}{\sqrt{2}a_W} = 2.98\%$ and $\Delta a_{bcc[001]} = \frac{a_W - a_{Co}}{a_W} = 20.79\%$, where $a_W$ and $a_{Co}$ are, respectively, the bulk bcc and hcp lattice parameters. Along the bcc[$\bar{1}$10] direction the Co is expected to grow pseudomorphically ($a_x = \sqrt{2}/2a_W$), up to 10 Co monolayers (1 ML $\simeq$ 0.2 nm) [20]. Along the bcc[001] direction, the misfit instead is large, implying that the Co structure relaxes for a thickness between 2 and 4 ML ($a_y = 3.56/4.56\frac{a_W}{2}$ [20]), with $a_x$ and $a_y$ defined in Fig. 1. Along the bcc[001] direction, the Co-W crystal forms a superstructure with a period of $14a_y$ (1.73 nm), reasonably smaller than the characteristic magnetic length scales even in ultrathin Co films. From the micromagnetic point of view the system can thus be considered uniform with averaged quantities and with a $C_{2v}$ symmetry.

Finally, a 2-nm-thick fcc Au(111) cap layer is deposited in order to promote out-of-plane anisotropy and protect the stack from oxidation. This layer has a $C_{6v}$ symmetry due to the fcc Au(111) surface twins. GIXRD measurements show that the W\Co interface is hardly modified by the capping layer [19] and the stressed Co layer does not significantly change its crystal symmetry. Hence we expect the contribution of the Au/Co interface to the in-plane anisotropic properties to be negligibly small.

## III. BRILLOUIN LIGHT SCATTERING SPECTROSCOPY

Brillouin light scattering spectroscopy was performed in the Damon-Eshbach (DE) configuration [21]. This technique is particularly suited for the study of anisotropic systems because it allows us to extract the magnetic properties independently along any direction. An external magnetic field $H_{ext}$ saturates the magnetization along an in-plane direction. A laser beam ($\lambda = 532$ nm) strikes the sample in the plane perpendicular to the magnetic field with an incidence angle $0^\circ < \theta_{inc} < 60^\circ$ in order to vary the spin-wave (SW) wave vector involved in the scattering process $k_{SW} = 4\pi\sin(\theta)/\lambda$. We call $\alpha$ the angle between $\mathbf{k}_{SW}$ (the direction along which the magnetization varies) and the bcc[$\bar{1}$10] crystallographic direction (Fig. 1). A $2\times3$ pass Fabry-Pérot interferometer allows us to analyze the backscattered light and to study the Stokes (S) and anti-Stokes (AS) spectrum generated by the scattering process between the laser photons and the SWs for different $\alpha$ values. The BLS spectrum in systems with DMI can be separated into symmetric $[f_0 = (|f_S| + |f_{AS}|)/2]$ and an antisymmetric $[f_{anti} = (|f_S| - |f_{AS}|)/2]$ components. The study of $f_0$ with $H_{ext}$ along the main crystallographic directions allows us to estimate the magnetocrystalline anisotropy (MCA) constants $K_i$ in the direction of the applied field, while $f_{anti}$ allows us to extract the sign and strength of the DMI acting on a Néel spin cycloid along the SW wave vector.

The $C_{2v}$ supercrystal symmetry induces a biaxial MCA energy density that can be formulated in the second-order approximation including the out-of-plane shape anisotropy ($K_d = \frac{1}{2}\mu_0 M_s^2$):

$$E_{anisotropy} = -(K_{out} - K_d)\cos^2\theta - K_{in}\sin^2\theta\,\cos^2\phi, \quad (2)$$

where $\theta$ and $\phi$ describe the magnetization direction (Fig. 1) and $K_{out}$ and $K_{in}$ are the out-of-plane and in-plane easy-axis MCA constants. The symmetric frequencies $f_0^{[001]}$ and $f_0^{[\bar{1}10]}$, when $H_{ext}$ is respectively applied along [001] and [$\bar{1}$10], can be calculated [22] as

$$f_0^{[001]} = \frac{\gamma\mu_0}{2\pi}\sqrt{\left[H_{ext}^{[001]} - H_{in} + Jk_{SW}^2 + P(k_{SW}t)M_s\right]\left[H_{ext}^{[001]} - H_{out} + Jk_{SW}^2 - P(k_{SW}t)M_s\right]}, \quad (3)$$

$$f_0^{[\bar{1}10]} = \frac{\gamma\mu_0}{2\pi}\sqrt{\left[H_{ext}^{[\bar{1}10]} + H_{in} + Jk_{SW}^2 + P(k_{SW}t)M_s\right]\left[H_{ext}^{[\bar{1}10]} - H_{out} + H_{in} + Jk_{SW}^2 - P(k_{SW}t)M_s\right]}, \quad (4)$$

where $\gamma$ is the gyromagnetic ratio; $J = \frac{2A}{\mu_0 M_s}$ is the SW stiffness, with $A$ being the exchange stiffness and $M_s$ being the spontaneous magnetization; and $P(k_{SW}t) = 1 - \frac{1-\exp(-|k_{SW}|t)}{|k_{SW}|t}$ is a geometric factor associated with the SW dynamics, with $t$ being the sample thickness. Following Eq. (2), we define $H_{out}$ and $H_{in}$ as the anisotropy fields. $H_{out}$ is the magnetic field needed to saturate the magnetization along the in-plane hard axis ($\theta = \pi/2; \phi = \pi/2$). $H_{in}$ is the difference between the fields needed to saturate the magnetization along

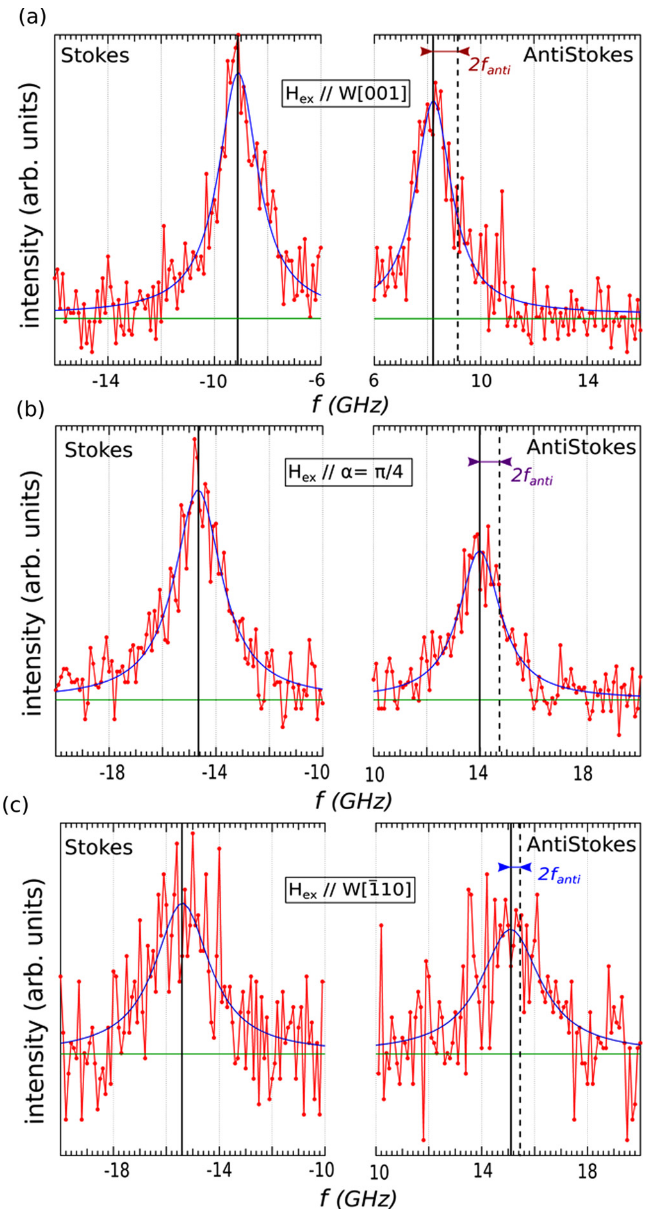


FIG. 2. BLS spectra on Au/Co(0.65 nm)/W(110) with $\mathbf{k}_{\mathrm{SW}}$ along the two in-plane symmetry axes. Red line: experimental data. Blue line: data fit with Lorentzian functions. Green line: background fit. In the AS spectra, the distance between the solid and dashed black lines shows the frequency shift between S and AS peaks. (a) BLS spectrum with $\mu_0 H_{\mathrm{ext}} = 0.6\,\mathrm{T}$ parallel to the bcc[001] axis and $k_{\mathrm{SW}} = 8.08/\mu\mathrm{m}$ parallel to the bcc[$\bar{1}$10] axis. (b) BLS spectrum with $\mu_0 H_{\mathrm{ext}} = 0.6\,\mathrm{T}$ along the direction with an angle of $\pi/4$ with respect to the bcc[1$\bar{1}$0] axis and $k_{\mathrm{SW}} = 18.09/\mu\mathrm{m}$. (c) BLS spectrum with $\mu_0 H_{\mathrm{ext}} = 0.5\,\mathrm{T}$ parallel to the bcc[$\bar{1}$10] axis and $k_{\mathrm{SW}} = 18.09/\mu\mathrm{m}$ parallel to the bcc[001] axis.

the in-plane easy axis ($\theta = \pi/2; \phi = 0$) and the in-plane hard axis. Analyzing the spectra in Fig. 2 can give a numerical estimation of the MCA constants.

In this work, the S-AS peaks occur for small values of $k_{\mathrm{SW}}$, i.e., $Jk_{\mathrm{SW}}^2 \ll H_{\mathrm{ext}}$, so that it is possible to neglect exchange contributions to the resonance BLS peaks. The spontaneous magnetization ($M_{\mathrm{s}} = 1.15 \times 10^6$ A/m) is inferred from the

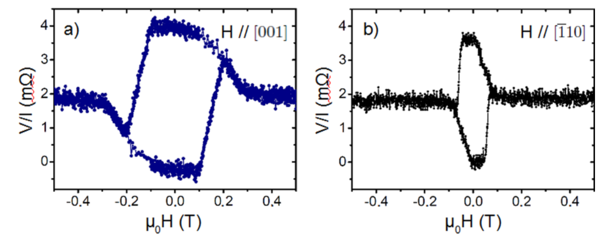


FIG. 3. Anomalous Hall effect measurements of the Au/Co(0.65 nm)/W(110) sample with the magnetic field applied along (a) the bcc[001] and (b) bcc[$\bar{1}$10] in-plane directions.

out-of-plane hysteresis loop obtained with a vibrating sample magnetometer (VSM). Evaluating $f_0^{[001]} = 8.53\,\mathrm{GHz}$ and $f_0^{[\bar{1}10]} = 15.24\,\mathrm{GHz}$ with $\mu_0 H_{\mathrm{ext}}^{[001]} = 0.6$ T and $\mu_0 H_{\mathrm{ext}}^{[\bar{1}10]} = 0.5$ T, respectively, we obtain $K_{\mathrm{in}} = \frac{1}{2}\mu_0 M_{\mathrm{s}} H_{\mathrm{in}} = 136\,\mathrm{kJ/m^3}$ ($\mu_0 H_{\mathrm{in}} = 0.24\,\mathrm{T}$) and $K_{\mathrm{out}} - K_{\mathrm{d}} = \frac{1}{2}\mu_0 M_{\mathrm{s}} H_{\mathrm{out}} = 199\,\mathrm{kJ/m^3}$ ($\mu_0 H_{\mathrm{out}} = 0.35\,\mathrm{T}$). Anomalous Hall effect measurements performed on the same sample with in-plane fields along the bcc[$\bar{1}$10] ($\theta = \pi/2; \phi = 0$) and bcc[001] ($\theta = \pi/2; \phi = \pi/2$) directions give saturation fields $\mu_0(H_{\mathrm{out}} - H_{\mathrm{in}}) \approx 0.1$ T and $\mu_0 H_{\mathrm{out}} \approx 0.3$ T, in good agreement with the anisotropy values (Fig. 3). Note that published results on the same system [23] showed a comparable out-of-plane anisotropy but a larger in-plane anisotropy.

The difference $2f_{\mathrm{anti}}$ arises from the different effects of DMI on SW modes with opposite $\mathbf{k}_{\mathrm{SW}}$ [24,25]. In ultrathin films DMI is the only physical phenomenon liable to break the S-AS peak symmetry [25]. BLS is thus particularly suited for the investigation of anisotropic DMI, especially because the extracted data are independent of any other anisotropy present in the system such as MCA and of the strength of $H_{\mathrm{ext}}$. The SW frequency shift in a system with interfacial DMI [$D(t) = D_s/t$)] in the DE geometry can be formulated as [24,26]

$$2f_{\mathrm{anti}} = \frac{2\gamma}{\pi}\frac{D(t)}{M_{\mathrm{s}}}k_{\mathrm{SW}} = \frac{2\gamma}{\pi}\frac{D_s}{M}k_{\mathrm{SW}}\,. \qquad (5)$$

$M$, the magnetic moment per unit surface ($M = M_{\mathrm{s}}\,t$), is obtained directly from VSM measurements, allowing a thickness-independent determination of the DMI strength $D_{\mathrm{s}}$. In Fig. 4 $2f_{\mathrm{anti}}$ is plotted as a function of $k_{\mathrm{SW}}$ along the main axes (bcc[001] and bcc[$\bar{1}$10]) and along an intermediate direction ($\alpha = \pi/4$). The points in the plot are extracted from the center of the Lorentzian distribution used to fit the S and AS peaks (Fig. 2). The error bars ($\delta f$) are obtained with a Levenberg-Marquardt error algorithm.

The plot in Fig. 4 demonstrates that along all directions $2f_{\mathrm{anti}}$ has a positive value, showing that the DMI promotes a clockwise spin chirality. Such a clockwise chirality (positive value of $D$) is in agreement with results for sputtered MgO/CoFeB/W samples [27] and is opposite to the chirality in AlOx/Co/Pt films [28,29]. Moreover, the DMI is strongly anisotropic. In the table in Fig. 4(a) the values of $D_{\mathrm{s}}$ along different crystallographic directions are shown. The DMI strength is a factor 2 to 3 higher along bcc[$\bar{1}$10] than along bcc[001], even taking into account the large error bar along the [001] direction. This difference is confirmed by

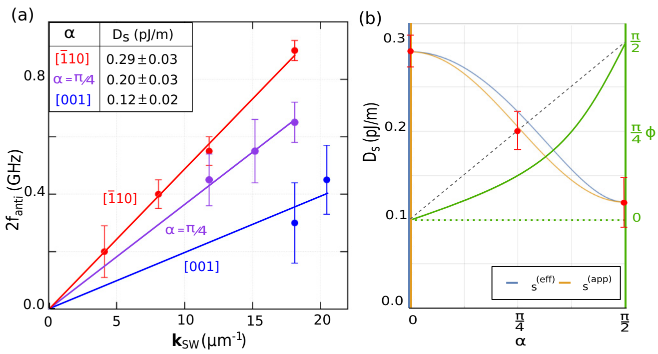


FIG. 4. (a) S-AS frequency shift $2f_{\text{anti}}$ as a function of the SW wave vector $k_{\text{SW}}$ for different in-plane directions $\alpha$. The dots are the experimental data, and the lines are linear fits yielding the DMI strength $D_s$. (b) Blue and orange lines: micromagnetic calculated $D_s^{(\text{eff})}$ [Eq. (10)] and $D_s^{(\text{app})}$ [Eq. (8)] as a function of the in-plane direction $\alpha$ (left axis); red dots: $D$ strength evaluated from the experimental data; green line: micromagnetic calculated magnetization direction promoted by DMI [Eq. (9)] as a function of the crystallography directions (right axis); dashed line: Néel-like cycloid.

the intermediate value found for the DMI strength for SWs propagating along the intermediate angle $\alpha = \pi/4$.

## IV. DMI AND CRYSTAL SYMMETRY: MICROMAGNETIC CALCULATIONS

Experimentally, we have thus found a 2–3 times larger DMI along the $[\bar{1}10]$ in-plane direction than along the [001] in-plane direction. In order to understand the relation between the crystal symmetry, the micromagnetic DMI anisotropy, and the symmetry of the spin modulation $\phi(\alpha)$ we developed micromagnetic calculations. Our approach does not aim at the quantitative evaluation of the DMI but allows illustrating how the $C_{2v}$ crystal symmetry sets constraints on the atomic DMI vectors $d_{ij}$ and how to obtain the anisotropic micromagnetic $D$ constants. It is valid if the analyzed magnetic configurations have a characteristic length $l$ much larger than the supercell parameter ($14a_y$). Indeed, it allows considering averaged $\langle \mathbf{d}_{ij} \rangle$ on the whole superlattice and describing the magnetization in a continuous-medium approach. The symmetry in a $C_{2v}$ crystal is not high enough to set uniquely the $\langle \mathbf{d}_{ij} \rangle$ vectors [2] but imposes their directions in the crystal plane and their mutual relationships [19]. The $\langle \mathbf{d}_{02} \rangle$ vector is perpendicular to its bond, whereas $\langle \mathbf{d}_{01} \rangle$ and $\langle \mathbf{d}_{01'} \rangle$ have the same strength $d$ and supplementary angles ($\delta_{01} + \delta_{01'} = \pi$) with respect to their bonds (see Fig. 1). Using the notation of the Lifshitz invariants $L_{jk}^{(i)} = m_j \frac{\partial m_k}{\partial i} - m_k \frac{\partial m_j}{\partial i}$, the micromagnetic DM energy can be written as

$$E_{DM} = -\int \left(D_s^{(x)} L_{xz}^{(x)} + D_s^{(y)} L_{yz}^{(y)}\right) d^2r, \tag{6}$$

with $D_s^{(x)} = \frac{d}{a}\frac{\sin(\beta+\delta_{01})}{\sin\beta}$ and $D_s^{(y)} = \frac{2d}{a}\left[\frac{\cos(\beta+\delta_{01})}{\cos\beta} - \frac{\langle d_{02} \rangle}{d}\frac{1}{\cos\beta}\right]$ (see Fig. 1). These relations show that knowing the crystal structure and the micromagnetic DMI is not sufficient to determine all $\langle \mathbf{d}_{ij} \rangle$ vectors.

In order to understand $\phi(\alpha)$ allowed in a general $C_{2v}$ system we formulate the DMI energy of a unidimensional spin modulation propagating along $\widehat{u}$ in the basis $(\widehat{u},\widehat{v},\widehat{z})$, turned at an angle $\alpha = (\widehat{x},\widehat{u})$ with respect to the crystal basis [Fig. 1(c)]:

$$\begin{aligned} E_{DM}(\alpha) = &-\int \left[\cos^2(\alpha) D_s^{(x)} + \sin^2(\alpha) D_s^{(y)}\right] L_{uz}^{(u)} d^2r \\ &-\int \left(D_s^{(x)} - D_s^{(y)}\right)\cos(\alpha)\sin(\alpha) L_{vz}^{(u)} d^2r. \end{aligned} \tag{7}$$

$E_{DM}(\alpha)$ presents two different types of Lifshitz invariants that describe a DMI stabilizing different spin modulations [4]. The first term, $L_{uz}^{(u)}$, describes the well-known result of an interfacial DMI promoting a Néel cycloid. The second term, $L_{vz}^{(u)}$, evidences that the interfacial DMI can stabilize a Bloch helicoid. This component vanishes along the main axes and has maxima proportional to the difference of the DMI constants $(D_s^{(x)} - D_s^{(y)})$ when $\alpha = \pi/4 + n\pi/2$. This means that in a general $C_{2v}$ system the DMI promotes Néel cycloids along the main axes and a mixed configuration between a Néel cycloid and a Bloch helicoid along the intermediate directions.

Equation (7) allows us first to calculate the apparent DMI constant $D_s^{(\text{app})}$ [19], defined as the DMI component acting on the DE spin wave, as a function of the in-plane propagation direction. In the DE geometry a SW propagating along $\hat{\mathbf{u}}$ can be described as $\mathbf{m}(u) = \mathbf{M} + \delta\mathbf{m}(u,t)$, where $\mathbf{M} \parallel \widehat{v}$ is imposed by $\mathbf{H}_{\text{ext}}$. The component $\delta\mathbf{m}(u,t)$, which represents the magnetization-varying part, is a Néel cycloid lying in the $(\widehat{u},\widehat{z})$ plane. Then $D_s^{(\text{app})}$ calculated from the DMI energy density of the SW reads, as a function of $\alpha$ [19],

$$D_s^{(\text{app})} = D_s^{(x)}\cos^2\alpha + D_s^{(y)}\sin^2\alpha. \tag{8}$$

Equation (8), plotted in Fig. 4(b), matches well the experimental data. It corresponds to only the first part of Eq. (7) due to the fact that $\delta\mathbf{m}$ describes a cycloid. Measuring the second part of Eq. (7) would require changing the measurement geometry and turning the optical plane by $\pi/2$ to get SWs propagating along the field direction [$\mathbf{M}$ along $\widehat{u}$ and $\delta\mathbf{m}(u,t)$ in the $(\widehat{v},\widehat{z})$ plane], with $\delta\mathbf{m}$ describing a helicoid.

## V. SKYRMIONS AND ANTISKYRMIONS

The competition between the first and second parts in Eq. (7) implies that along an arbitrary direction, spin spirals (or, equivalently, domain walls) may be intermediate between Néel and Bloch spirals. Writing $\phi$ as the angle between the spiral modulation plane and the $\widehat{x}$ axis, we minimize the DMI energy to find the optimum modulation plane. As a function of the propagation direction, we obtain

$$\tan\phi = \left(\frac{D_s^{(y)}}{D_s^{(x)}}\right)\tan\alpha, \tag{9}$$

with an effective DMI constant that maximizes the DMI energy gain:

$$\begin{aligned} D_s^{\text{eff}} = &\, D_s^{(x)}\cos\alpha\,\cos\left[\arctan\left(\frac{D_s^{(y)}}{D_s^{(x)}}\tan\alpha\right)\right] \\ &+ D_s^{(y)}\sin\alpha\,\sin\left[\arctan\left(\frac{D_s^{(y)}}{D_s^{(x)}}\tan\alpha\right)\right]. \end{aligned} \tag{10}$$

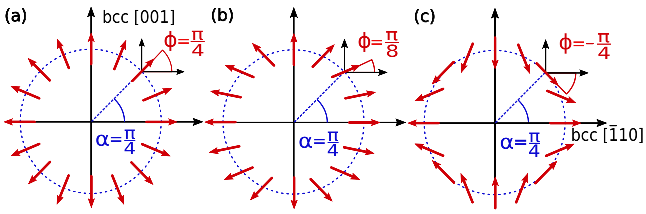


FIG. 5. Polar plot of the magnetization direction $\phi$ promoted by DMI as a function of the in-plane direction of variation $\alpha$ [Eq. (9)] for different ($D_s^{(x)}$; $D_s^{(y)}$) values: (a) $D_s^{(x)} = D_s^{(y)}$, (b) $D_s^{(x)} = 2.5D_s^{(y)}$, and (c) $D_s^{(x)} = -D_s^{(y)}$.

Setting $D_s^{(x)} = 2.5D_s^{(y)}$, it is possible to obtain $D_s^{(\mathrm{eff})}(\alpha)$ for Au/Co/W(110) [Figs. 2(b) and 5(b)]. As predicted from Eq. (7), along the main axes $D_s^{(\mathrm{eff})} = D_s^{(\mathrm{app})}$, and the spin spiral is purely Néel; the largest mismatch between $D_s^{(\mathrm{eff})}$ and $D_s^{(\mathrm{app})}$ occurs along $\alpha = \pi/4$.

The discussion can be generalized for different $D_s^{(x)}/D_s^{(y)}$ ratios, and we emphasize two interesting cases. First, setting isotropic conditions ($D_s^{(x)} = D_s^{(y)}$), we obtain the well-known result of a DMI stabilizing only Néel spirals [$\phi(\alpha) = \alpha$]. In the other extreme, $D_s^{(x)} = -D_s^{(y)}$ implies $\phi(\alpha) = -\alpha$, so Néel cycloids are stabilized along the main crystallographic directions, and purely Bloch helicoids are stabilized at $\alpha = \pi/4 + n\pi/2$. Considering localized textures such as bubbles, the energy minimization remains valid, and different types of textures can be expected, as depicted in Fig. 5 for $D_s^{(x)}/D_s^{(y)} = 1$, 2.5, and $-1$ [30]. Considering the winding number $W = [\phi(\alpha)]_{\alpha=0}^{\alpha=2\pi}/2\pi$, the first two textures depict skyrmions (although in the second case we may expect distortions) with $W = 1$, while the third case, with $W = -1$, has the signature of an antiskyrmion [5].

In order to experimentally achieve a system with opposite signs of $D$ along two perpendicular in-plane directions, one possibility would be to replace the Au cover layer in our sample with a heavy-metal (HM) layer inducing a DMI at the HM/Co interface with a sign opposite to the DMI at the Co/W interface. This DMI could be isotropic and should have a strength in between the values found along the bcc[$\bar{1}$10] and bcc[001] directions in the Au/Co/W(110) system. Another possibility would be to use a system suggested recently in a theoretical paper discussing anisotropic DMI and antiskyrmions in Fe/W(110) [31].

## VI. CONCLUSIONS

We have investigated DMI in an out-of-plane magnetized epitaxial Au/Co(0.65 nm)/W(110) trilayer. The DMI in this system promotes a clockwise chirality of the spin modulation with a DMI strength 2–3 times larger along bcc[$\bar{1}$10] than along bcc[001]. This anisotropy arises from the $C_{2v}$ symmetry of the Co/W(110) stack. We used a micromagnetic model to highlight the link between the atomic DMI at the Co/W(110) interface, based on its expected superlattice, and the resulting micromagnetic anisotropic DMI. The DMI is expected to give rise not only to Néel cycloids but to mixed cycloid/helicoid textures [Fig. 5(b)]. The experimental evidence of a strongly anisotropic DMI is the first important step for stabilization in a magnetic thin film of deformed isolated skyrmions and antiskyrmions.

## ACKNOWLEDGMENTS

We express our thanks to P. David and V. Guisset for crucial support in the sample growth. We acknowledge a grant from the Laboratoire d'excellence LANEF in Grenoble (Grant No. ANR-10-LABX-51-01) and support from the ANR (Grant No. ANR-14-CE26-0012 ULTRASKY) and from the government of the Russian Federation (Grant No. 074-U01). We thank A. Wartelle, S. Blügel, B. Zimmermann, and M. Hoffmann for helpful discussions and U. Rössler for useful correspondence. We acknowledge the European Synchrotron Radiation Facility and the french CRG-IF beamline for providing beam time.

[1] I. Dzyaloshinskii, Sov. Phys. JETP **5**, 1259 (1957).
[2] T. Moriya, Phys. Rev. **120**, 91 (1960).
[3] A. Fert and P. M. Levy, Phys. Rev. Lett. **44**, 1538 (1980).
[4] A. N. Bogdanov and U. K. Rößler, Phys. Rev. Lett. **87**, 037203 (2001).
[5] N. Nagaosa and Y. Tokura, Nat. Nanotechnol. **8**, 899 (2013).
[6] A. Bogdanov and D. Yablonskii, Zh. Eksp. Teor. Fiz. **96**, 253 (1989).
[7] M. Kataoka and O. Nakanishi, J. Phys. Soc. Jpn. **50**, 3888 (1981).
[8] S. Mühlbauer, B. Binz, F. Jonietz, C. Pfleiderer, A. Rosch, A. Neubauer, R. Georgii, and P. Böni, Science **323**, 915 (2009).
[9] N. Romming, C. Hanneken, M. Menzel, J. E. Bickel, B. Wolter, K. von Bergmann, A. Kubetzka, and R. Wiesendanger, Science **341**, 636 (2013).
[10] C. Moreau-Luchaire, C. Moutafis, N. Reyren, J. Sampaio, C. A. F. Vaz, N. Van Horne, K. Bouzehouane, K. Garcia, C. Deranlot, P. Warnicke *et al.*, Nat. Nanotechnol. **11**, 444 (2016).
[11] O. Boulle, J. Vogel, H. Yang, S. Pizzini, D. de Souza Chaves, A. Locatelli, T. O. Mentes, A. Sala, L. D. Buda-Prejbeanu, O. Klein *et al.*, Nat. Nanotechnol. **11**, 449 (2016).
[12] J. Hagemeister, E. Y. Vedmedenko, and R. Wiesendanger, Phys. Rev. B **94**, 104434 (2016).
[13] U. Güngördü, R. Nepal, O. A. Tretiakov, K. Belashchenko, and A. A. Kovalev, Phys. Rev. B **93**, 064428 (2016).
[14] P.-J. Hsu, A. Kubetzka, A. Finco, N. Romming, K. von Bergmann, and R. Wiesendanger, Nat. Nanotechnol. **12**, 123 (2016).
[15] K. Shibata, J. Iwasaki, N. Kanazawa, S. Aizawa, T. Tanigaki, M. Shirai, T. Nakajima, M. Kubota, M. Kawasaki, H. S. Park *et al.*, Nat. Nanotechnol. **10**, 589 (2015).
[16] B. Dupé, C. N. Kruse, T. Dornheim, and S. Heinze, New J. Phys. **18**, 055015 (2016).
[17] W. Koshibae and N. Nagaosa, Nat. Commun. **7**, 10542 (2016).
[18] O. Fruchart, S. Jaren, and J. Rothman, Appl. Surf. Sci. **135**, 218 (1998).

[19] See Supplemental Material at http://link.aps.org/supplemental/10.1103/PhysRevB.95.214422, which gives details of the sample growth and calculations and includes Refs. [32–37].
[20] H. Fritzsche, J. Kohlhepp, and U. Gradmann, Phys. Rev. B **51**, 15933 (1995).
[21] R. Damon and J. Eshbach, J. Phys. Chem. Sol. **19**, 308 (1961).
[22] L. Baselgia, M. Warden, F. Waldner, S. L. Hutton, J. E. Drumheller, Y. Q. He, P. E. Wigen, and M. Maryško, Phys. Rev. B **38**, 2237 (1988).
[23] R. Sellmann, H. Fritzsche, H. Maletta, V. Leiner, and R. Siebrecht, Phys. Rev. B **64**, 054418 (2001).
[24] K. Zakeri, Y. Zhang, J. Prokop, T.-H. Chuang, N. Sakr, W. X. Tang, and J. Kirschner, Phys. Rev. Lett. **104**, 137203 (2010).
[25] A. A. Stashkevich, M. Belmeguenai, Y. Roussigné, S. M. Cherif, M. Kostylev, M. Gabor, D. Lacour, C. Tiusan, and M. Hehn, Phys. Rev. B **91**, 214409 (2015).
[26] L. Udvardi and L. Szunyogh, Phys. Rev. Lett. **102**, 207204 (2009).
[27] J. Torrejon, J. Kim, J. Sinha, S. Mitani, M. Hayashi, M. Yamanouchi, and H. Ohno, Nat. Commun. **5**, 4655 (2014).
[28] M. Belmeguenai, J.-P. Adam, Y. Roussigné, S. Eimer, T. Devolder, J.-V. Kim, S. M. Cherif, A. Stashkevich, and A. Thiaville, Phys. Rev. B **91**, 180405 (2015).
[29] S. Pizzini, J. Vogel, S. Rohart, L. D. Buda-Prejbeanu, E. Jué, O. Boulle, I. M. Miron, C. K. Safeer, S. Auffret, G. Gaudin *et al.*, Phys. Rev. Lett. **113**, 047203 (2014).
[30] B. Zimmermann, M. Heide, G. Bihlmayer, and S. Blügel, Phys. Rev. B **90**, 115427 (2014).
[31] M. Hoffmann, B. Zimmermann, G. P. Müller, D. Schürhoff, N. S. Kiselev, C. Melcher, and S. Blügel, arXiv:1702.07573.
[32] M. Pratzer, H. J. Elmers, and M. Getzlaff, Phys. Rev. B **67**, 153405 (2003).
[33] J. H. van der Merwe, E. Bauer, D. L. Tonsing, and P. M. Stoop, Phys. Rev. B **49**, 2127 (1994).
[34] S. Andrieu, C. Chatelain, M. Lemine, B. Berche, and P. Bauer, Phys. Rev. Lett. **86**, 3883 (2001).
[35] G. Garreau, M. Farle, E. Beaurepaire, and K. Baberschke, Phys. Rev. B **55**, 330 (1997).
[36] M. A. Ruderman and C. Kittel, Phys. Rev. **96**, 99 (1954).
[37] P. Moras, G. Bihlmayer, P. M. Sheverdyaeva, S. K. Mahatha, M. Papagno, J. Sánchez-Barriga, O. Rader, L. Novinec, S. Gardonio, and C. Carbone, Phys. Rev. B **91**, 195410 (2015).